catalysts

MDPI

Article

Effect of Support on Complete Hydrocarbon Oxidation over Pd-Based Catalysts

Tatyana Tabakova [1,*], Bozhidar Grahovski [1], Yordanka Karakirova [1], Petya Petrova [1], Anna Maria Venezia [2], Leonarda Francesca Liotta [2] and Silviya Todorova [1,3,*]

[1] Institute of Catalysis, Bulgarian Academy of Sciences, Acad. G. Bonchev St., Bldg. 11, 1113 Sofia, Bulgaria; grahovski@ic.bas.bg (B.G.); danieper@ic.bas.bg (Y.K.); petia@ic.bas.bg (P.P.)
[2] Istituto per lo Studio dei Materiali Nanostrutturati, CNR, Via Ugo La Malfa, 153, 90146 Palermo, Italy; annamaria.venezia@cnr.it (A.M.V.); leonardafrancesca.liotta@cnr.it (L.F.L.)
[3] National Centre of Excellence Mechatronics and Clean Technologies, Kliment Ohridski Blvd., 8, 1756 Sofia, Bulgaria
* Correspondence: tabakova@ic.bas.bg (T.T.); todorova@ic.bas.bg (S.T.)

Abstract: Developing efficient strategies for VOC emission abatement is an urgent task for protection of the environment and human health. Complete catalytic oxidation exhibits advantages, making it an effective, environmentally friendly, and economically profitable approach for VOC elimination. Pd-based catalysts are known as highly active for hydrocarbon catalytic oxidation. The nature of carrier materials is of particular importance because it may affect activity by changing physicochemical properties of the palladium species. In this work, Al_2O_3, CeO_2, CeO_2-Al_2O_3, and Y-doped CeO_2-Al_2O_3 were used as carriers of palladium catalysts. Methane and benzene were selected as representatives of two types of hydrocarbons. A decisive step in complete methane oxidation is the first C–H bond breaking, while the extraordinary stability of the six-membered ring structure is a challenge in benzene oxidation. The support effect was explored by textural measurements using XRF, XRD, XPS, EPR, and TPR techniques. Three ceria-containing samples showed superior CH_4 oxidation performance, achieving 90% methane conversion at about 300 °C and complete oxidation at 320 °C. Evidence for presence of Pd^{2+} species in all samples regarded as most active was provided by XP-derived analysis. Pd/Y-Ce/Al catalysts exhibited very high activity in benzene oxidation by reaching 100% conversion at 180 °C. The contributions of higher Pd and Ce^{3+} surface concentrations, the presence of O_2^--adsorbed superoxo species, and $Pd^0 \leftrightarrow PdO$ redox transfer were considered. The potential of a simple, environmentally friendly, and less energy demanding mechanochemical preparation procedure of mixed oxides was demonstrated.

Keywords: Pd-based catalyst; CH_4 oxidation; complete benzene oxidation; mechanochemical synthesis; CeO_2-Al_2O_3; Y_2O_3-doped CeO_2-Al_2O_3

check for updates

Received: 16 December 2024
Revised: 17 January 2025
Accepted: 21 January 2025
Published: 23 January 2025

Citation: Tabakova, T.; Grahovski, B.; Karakirova, Y.; Petrova, P.; Venezia, A.M.; Liotta, L.F.; Todorova, S. Effect of Support on Complete Hydrocarbon Oxidation over Pd-Based Catalysts. *Catalysts* **2025**, *15*, 110. https://doi.org/10.3390/catal15020110

Copyright: © 2025 by the authors. Licensee MDPI, Basel, Switzerland. This article is an open access article distributed under the terms and conditions of the Creative Commons Attribution (CC BY) license (https://creativecommons.org/licenses/by/4.0/).

1. Introduction

Nowadays, atmospheric pollution represents a serious concern with respect to human health and ecosystems. It is closely related to climate change and some effects of global warming that have occurred faster than scientists have predicted [1,2]. Volatile organic compounds (VOCs) are an important class of air pollutants in urban and industrial areas. Some of the main sources of VOC emissions are automobile exhaust, industrial and energetic processes, combustion by-products, and residential activities [3–5]. Among VOCs, benzene, toluene, ethylbenzene, and xylene belong to a group of compounds known as

BTEX and are regarded as the most common aromatic VOCs, with significant contributions to industrial emissions. Using natural gas, primarily composed of methane, is an effective method to reduce the concentration of pollutants emitted by gasoline- or diesel-fueled vehicles and stationary power generation facilities. However, the release of unburned methane from vehicles and gas power plants, as well as leakage during production and transportation, is considered a major drawback due to methane's stronger detrimental greenhouse effect compared to CO_2 [6]. In December 2019, the European Commission adopted the so-called Green Deal, also known as the Green Pact, which is a package of policies aimed at making Europe climate-neutral by 2050. EC strategies and initiatives target the reduction of greenhouse gas production at least by 50% compared to 1990 levels, as well as zero pollution by 2050 with respect to air, soil, and water. Horizon Europe, a key seven-year EU funding program for research and innovation, was established for this ambitious purpose for the period of 2021–2027. Climate technologies will receive 35% of the funding amount for Horizon Europe. In this context, VOC emissions abatement is a particularly pertinent problem for future research.

Catalytic oxidation is the most efficient method for VOC and methane abatement in exhaust gases. It is widely used, owing to some important advantages, such as high catalytic activity and treatment efficiency, low energy consumption, and a lack of secondary pollutants [7–9]. A significant number of research studies have been devoted to catalyst design and composition optimization because of the decisive role of the catalyst in achieving high efficiency in environmental pollutants abatement. Some recent reviews highlight the effectiveness of Pd-based catalysts, which are recognized as highly active for the catalytic oxidation of hydrocarbons [10–12]. Along with Pd dispersion and the oxidation state, the physicochemical properties of the support significantly affect catalyst performance. The selection of a support is of particular importance because in many cases, the metal oxide plays ab active part in the reaction mechanism instead of being merely a carrier of the active phase. One consolidated strategy to develop cost-effective and high-performing catalyst formulations is the use of appropriate and economically viable supports. Alumina is widely applied for catalyst support in industry, owing to its low cost, high specific surface area, high thermal stability, and mechanical strength. An effective approach to stabilize PdO against decomposition, as well as to diminish Pd content and increase PdO surface exposure, is alumina modification by metal oxides [11]. Ceria has a high oxygen storage and release capacity due to its fast Ce^{4+}/Ce^{3+} redox cycle, motivating its use for the preparation of Ce-Al mixed oxide supports. Different compositions and synthesis methods have been reported. Wet impregnation of alumina with 1, 5, and 10 wt.% Ce favored coexistence between supported Pd^0 and PdO species, which improved benzene oxidation on $Pd/Ce\text{-}Al_2O_3$ [13]. Ramírez-López et al. employed the sol–gel method for the preparation of alumina modified by 2 to 50 wt.% CeO_2 [14]. Palladium-containing samples with 5, 10, and 15 wt.% ceria achieved 100% methane conversion at temperatures below 550 °C. Alumina consecutive wetness impregnation by changing the CeO_2 (17.5 wt.%) and Pd (1.5 wt.%) loading sequences affected palladium dispersion, influencing catalytic activity [15]. Samples with Ce added over Pd and Al_2O_3 demonstrated higher propane, NO, and CO conversion. Fertal et al. reported opposite findings by studying the impact of sequential impregnation of $PdO/CeO_2/Al_2O_3$ catalysts with 4 wt.% Pd and 20 wt.% CeO_2 on methane combustion [16]. The lower activity of samples prepared by impregnation of cerium nitrate on Pd/Al_2O_3 was attributed to strong PdO–ceria interactions and diminished access of methane and oxygen to active PdO sites. Commercial γ-alumina-supported Pd/CeO_2 colloidal assembled spheres with higher amounts of interfacial $Pd-O-Ce$ species and O_{ads} concentration than Pd/CeO_2 catalysts exhibited enhanced CH_4 combustion activity [17]. Recently, the effect of yttria modification on the activity of ceria-supported gold

catalysts in complete benzene oxidation (CBO) was studied [18]. The authors reported that ceria doped with 1 wt.% Y_2O_3 demonstrated the best performance, which was attributed to the role of support in the benzene activation stage, along with enhanced surface reoxidation. Later, bearing in mind the suitability of Pd-based catalysts for low-temperature VOC oxidation, the same authors reported that the addition of 1 wt.% Y_2O_3 to ceria produced an active and stable Pd-based catalyst for benzene oxidation due to an increased oxygen vacancy concentration and improved Pd dispersion [19]. However, the effect of Y doping of ceria on the activity of supported palladium catalysts in methane oxidation has not been examined. Yttrium ionic radius is suitable for insertion into ceria lattice with 0.97 Å for Ce^{4+} and 1.02 Å for Y^{3+} in eight-fold coordination. Moreover, the oxidation state of yttrium ions is appropriate for the formation of oxygen vacancies in order to compensate for the negative charge induced by $Ce^{4+} \rightarrow Y^{3+}$ substitution. Along with yttrium abundance, these two features motivated the study of Y-doped, CeO_2-Al_2O_3-supported, Pd-based catalysts.

The aim of this work is to explore the role of support for complete hydrocarbon oxidation over Pd-based catalysts. Methane and benzene were selected as representatives of two types of very stable hydrocarbon molecules. A decisive step in complete methane oxidation is the first C–H bond breaking because of its higher activation energy than C–C bonds [20], while the extraordinary stability of the six-membered ring structure is a challenge in benzene oxidation. A cost reduction strategy for catalyst production stimulated palladium deposition on γ-alumina modified by well surface-dispersed ceria and Y-doped ceria using mechanochemical mixing. This approach enabled the achievement of a higher interfacial area between the palladium nanoparticles and alumina-supported ceria. It is not a commonly applied routine method and could be considered a novelty. From an economic point of view, modifying the alumina surface with highly dispersed ceria provided further advantages—namely, it decreased the amount of ceria in the catalyst formulation as compared to Pd/CeO_2. To the best of our knowledge, palladium promotion on CeO_2-Al_2O_3 and Y-doped CeO_2-Al_2O_3 mixed oxides prepared by simple, less polluting, and energy-saving mechanochemical methods has not been studied in the benzene and methane oxidation reactions.

2. Results

2.1. Catalytic Activity Measurements

Four metal oxides, namely Al_2O_3, CeO_2, CeO_2-Al_2O_3, and Y-doped CeO_2-Al_2O_3, were selected as carriers of palladium catalysts. The notations of the various samples are described in the Experimental section. Methane conversion as a function of the reaction temperature is presented in Figure 1a. The calculated value for the standard deviation was ±1.5% based on the average of six measurements at each experimental point. Two successive measurements were necessary to determine average values for the conversion degree. All samples demonstrated a progressive activity increase with increasing temperature. However, a favorable role of ceria as support was observed. Palladium on ceria and alumina-supported ceria, namely Pd/CeO_2, Pd/CeAl, and Pd/Y-CeAl, behaved significantly better as compared to Pd/Al_2O_3. In fact, Pd/CeO_2 exhibited higher conversions in a lower temperature range. The three ceria-containing samples reached about 90% CH_4 conversion at 300 °C and complete oxidation at 320 °C vs. 60% at 300 °C and 100% at 390 °C with Pd/Al_2O_3. A comparison of "light off" profiles demonstrated that yttrium-doped ceria had no effect on oxidation activity. Considering economic profitability, the best trade-off was achieved with the Pd/CeAl sample, which showed comparable activity for lower ceria content.

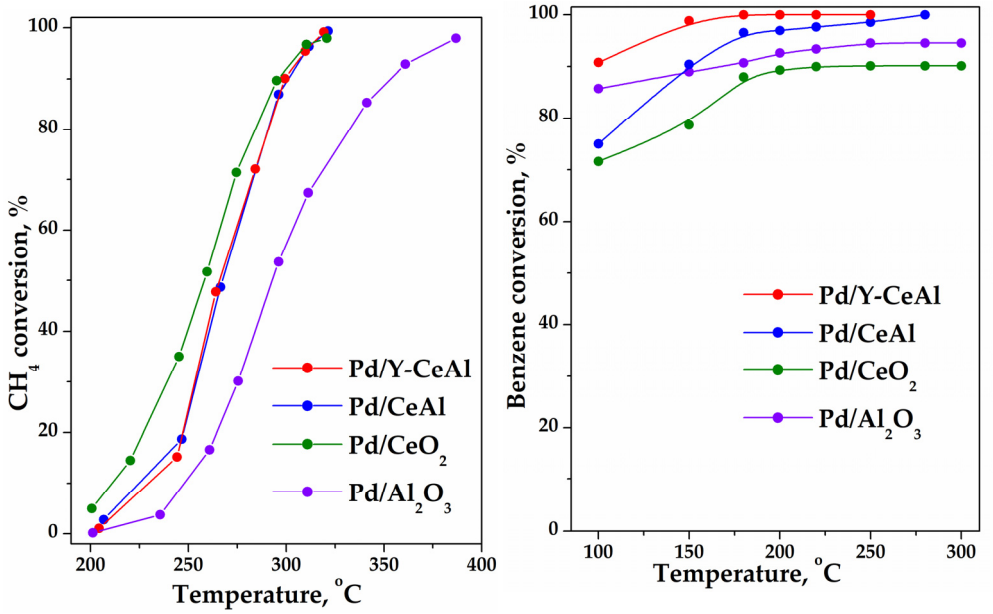


Figure 1. Catalytic performance of Pd-based catalysts with different supports: (**a**) CH_4 oxidation (inlet gas mixture: 1000 ppmv CH_4, 25 vol.% O_2; balanced up to 100% with N_2; flow rate of 20,000 h^{-1}); (**b**) benzene oxidation (inlet benzene concentration of 1314 ppm in air and space velocity of 4000 h^{-1}).

Table S1 presents comparative data about Pd-based catalysts used for complete methane oxidation. As can be seen, the catalysts developed in this work demonstrated high activity, achieving some of the lowest temperatures, such as 300 °C for 90% conversion. However, an assessment of the best-performing catalyst could not be conducted because of the diversity of catalyst compositions and experimental reaction conditions.

Long-term stability tests were not carried out; however, the establishment of steady-state activity for a certain reaction temperature took 1–2 h, while catalytic measurement of each sample continued for 3 days. Finally, the conversion remained complete within 2 h, and no activity decline was observed, indicating the stability of the catalysts.

Benzene oxidation activity is expressed as the benzene conversion degree. A quite different activity order was observed for benzene oxidation over the studied samples (Figure 1b). Contrary to the above-described results, Pd/Y-CeAl exhibited superior performance, achieving complete conversion at 180 °C. Products of incomplete oxidation were not registered within 24 h stability tests at this temperature. Preliminary measurements with some expected intermediate products of partial oxidation such as benzoquinone, phenol, maleic anhydride, and hydroxy-1,4-benzoquinone were carried out. These compounds were injected as evidence to detect the retention time under identical GC conditions. Pd/CeAl also showed high oxidation activity, achieving 96% conversion at 175 °C and complete conversion at 300 °C. The role of yttrium-doped ceria was clearly revealed by comparing the benzene conversion degree at 180 °C. An interesting finding was that Pd/Al_2O_3 performed better than Pd deposition on reducible CeO_2. A conversion of 85% was reached at 100 °C. However, it is worth noting that neither sample was able to achieve complete conversion, even at 300 °C. Table S2 presents a summary of the composition and catalytic performance of the Pd-based catalysts prepared in this work and reference literature. Pd/Y-CeAl significantly outperformed all catalysts, achieving the lowest T_{90} of 100 °C. However, as noted above, catalyst composition and experimental conditions were quite different, and a reliable conclusion could not be made. The table also reports data about catalysts evaluated using the same experimental setup. The Pd/Y-CeAl catalyst developed in this work demonstrated superior performance. A 90% conversion at 180 °C

and a beneficial impact of Pd deposition on Fe-doped ceria as compared with a matching Au-based sample (T_{90} = 200 °C) were observed [21]. Both catalysts showed a lower T_{90} relative to that of Pt loaded on Fe-modified fly ash zeolite X with T_{90} = 250 °C [22].

2.2. Catalyst Characterization

2.2.1. Chemical Composition

The actual chemical compositions of the samples determined by X-ray fluorescence spectrometry (XRF) are reported in Table 1. A homogenous structure was verified by similar values measured at three spots. Analysis indicated values very close to the target values for all components, revealing the suitability of mechanochemical mixing for sample preparation with preset loading. In all catalysts, the palladium content was very close to 1 wt.%, which confirmed that palladium deposition–precipitation was carried out successfully.

Table 1. Catalyst compositions measured by XRF.

Sample	Chemical Composition (wt.%)			
	Pd	**CeO_2**	**Y_2O_3**	**Al_2O_3**
Pd/Al_2O_3	1.03	-	-	98.97
Pd/CeO_2	1.10	98.90	-	-
Pd/CeAl	1.06	29.68	-	69.26
Pd/Y-CeAl	1.01	29.40	0.29	69.29

2.2.2. Textural Characteristics

Textural features of the samples, namely specific surface area (S_{BET}), pore volume (V_{pore}), and average pore size (D_{pore}), are listed in Table 2. Alumina-based samples are mesoporous materials with S_{BET} values close to those of γ-Al_2O_3 and pore sizes around 10 nm. In the case of modified alumina, namely Ce/Al and Y-doped Ce/Al, the S_{BET} and total pore volume showed a slight decrease that could be attributed to alumina mixing with ceria with a lower specific surface area, i.e., 63 $m^2\ g^{-1}$. The same trend in S_{BET} values was reported by Yang et al., who reported values of 144 and 46 $m^2\ g^{-1}$ and activity at T_{90} = 410 and 535 °C for $Pd/CeO_2/Al_2O_3$ and Pd/CeO_2 catalysts, respectively [17]. The preparation of a 4Pd-20CeO_2/Al_2O_3 sample by impregnating $Pd(NO_3)_2$ aqueous solution to an aqueous slurry of 20CeO_2/Al_2O_3 produced a catalytic material with an S_{BET} value of 117 $m^2\ g^{-1}$ [16].

Table 2. Textural characteristics, average size (D_{ceria}), and lattice parameter (α) of ceria estimated by XRD.

Sample	S_{BET} ($m^2\ g^{-1}$)	V_{pore} ($cm^3\ g^{-1}$)	D_{pore} (nm)	D_{ceria} (nm)	α_{ceria} (nm)
γ-Al_2O_3	200.0	0.53	10.6	-	-
Pd/Al_2O_3	195.8	0.52	9.7	-	-
CeO_2	63.0	0.29	20.3	6.3	0.5424 (2)
Pd/CeO_2	67.6	0.28	16.5	6.2	0.5424 (4)
Ce/Al	165.0	0.39	9.5	6.1	0.5422 (1)
Pd/CeAl	161.2	0.45	9.5	5.8	0.5424 (1)
Y-Ce/Al	168.0	0.43	10.0	6.1	0.5421 (2)
Pd/Y-CeAl	166.4	0.42	9.6	5.8	0.5420 (1)

The textural parameters of Pd-containing samples remained close to those of the used carriers. Recently, the textural properties of CeO_2–Al_2O_3 mixed oxides prepared by impregnation and mechanochemical mixing were studied [23]. A nearly two-fold lowering

of S_{BET} and the pore volume of impregnated samples was observed in comparison with bare γ-Al_2O_3, which was attributed to the deep penetration of Ce^{3+} ions into alumina pores. The formation of ceria crystallites inside the pores was found to be responsible for the limited access of reactants to active sites and the lower catalytic activity. In the present case, employment of mechanochemical mixing is favorable for preserving beneficial textural features of alumina.

2.2.3. X-Ray Powder Diffraction (XRD) Measurements

XRD analysis was carried out for phase composition identification of catalysts. The XRD patterns of γ-Al_2O_3, CeO_2, and supported Pd samples are shown in Figure 2. The positions and intensities of the peaks are very similar. Clearly visible diffraction lines at 2θ of 28.5°, 33.1°, 47.5°, and 56.4° were attributed to the (111), (200), (220), and (311) planes of ceria phase in the cubic crystal structure of the fluorite type, respectively. A weak contribution of Al_2O_3 was distinguishable at about 2θ = 38°, as well as a ceria peak shoulder at 2θ = 47.5°. No diffraction peaks ascribed to the presence of yttria or any palladium-related phases were discernible. This finding may be associated with small loadings, suggesting high dispersion.

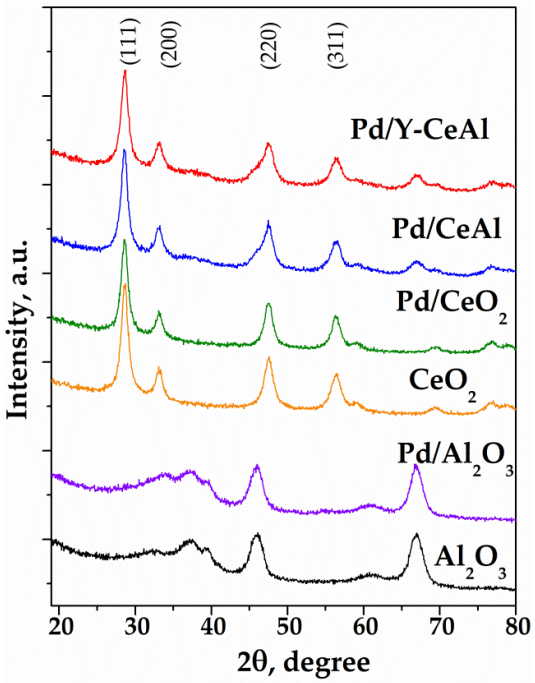


Figure 2. XRD patterns of γ-Al_2O_3-, CeO_2-, and Pd-based catalysts using various carriers.

The average size of ceria (D_{ceria}) estimated according to Scherer's equation using the FWHM of the peak at 2θ of 28.5° and the unit cell parameter (α_{ceria}) are reported in Table 2. All samples show very similar values. Analysis indicated that Pd deposition did not affect the particle size or the lattice parameter. Concerning yttrium doping, changes in the ceria unit cell parameter upon replacement of Ce with Y ions was not expected because of the similarity of the ionic radii: 0.97 Å for Ce^{4+} and 1.02 Å for Y^{3+} in eight-fold coordination.

2.2.4. X-Ray Photoelectron Spectroscopy (XPS) Measurements

The oxidation state at the surface of all samples was studied by XPS. Table 3 shows the results of quantitative XP spectral analysis. Al 2p binding energy (BE) is not listed because the peak was located at 75.1 ± 0.1 eV in the spectra of all samples. The BE of the Pd $3d_{5/2}$ peak in the range of 336.6–337.1 eV indicated the presence of Pd^{2+} in all palladium-containing samples (Figure 3). Higher values of XPS-derived data on the Pd/(Ce + Al)

atomic ratio, namely 0.044 and 0.041 for Pd/CeAl and Pd/Y-CeAl, respectively, as compared to the analytical value of 0.006 revealed a higher palladium dispersion on the surfaces of these samples. The highest atomic ratio of 0.14 calculated for Pd/CeO_2 reflects a lower ceria surface area, maximizing the Pd photoelectrons with respect to support-related photoelectrons. This value agrees well with the role of ceria in favoring a high dispersion of the supported noble metals.

Table 3. X-ray photoelectron spectral analysis.

Catalyst	Ce $3d_{5/2}$ (eV)	Pd $3d_{5/2}$ (eV)	Y $3d_{5/2}$ (eV)	Y/Pd	Pd/(Ce + Al)	$Ce^{3+}/(Ce^{3+} + Ce^{4+})$
Pd/Al_2O_3	-	336.7	-	-	0.017 0.048 *	-
Pd/CeO_2	881.7	337.1	-	-	0.140 0.0163 *	0.32
Pd/CeAl	881.8	336.6	-	-	0.044 0.0062 *	0.33
Pd/Y-CeAl	881.8	336.7	157.8	0.21 0.28 *	0.041 0.0063 *	0.40

* Analytical ratio.

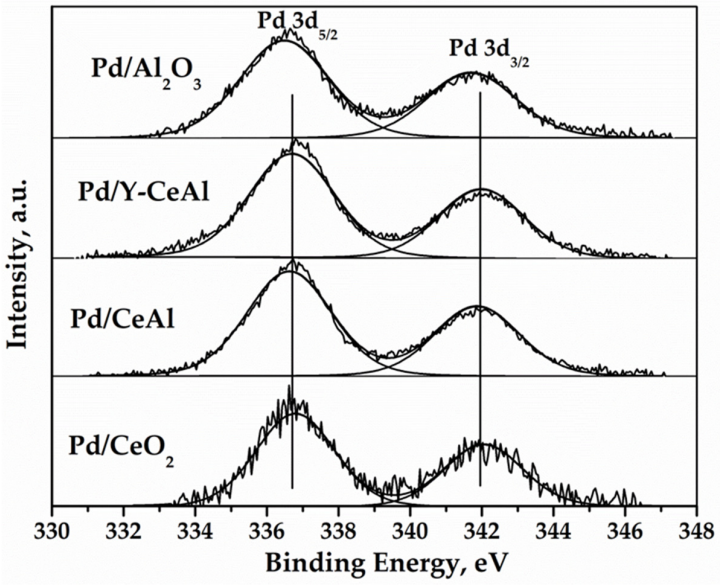


Figure 3. Pd 3D XP spectra of the studied catalysts.

Ceria oxidation states, namely Ce^{4+} and Ce^{3+}, were detected in the Ce 3d spectra of all Ce-containing samples (Figure S1). Based on the consensus about the relationship between Ce^{3+} concentration and oxygen vacancies formed for charge compensation, special attention was paid to the $Ce^{3+}/(Ce^{4+} + Ce^{3+})$ atomic ratio. The values were in the interval of 0.25–0.38, i.e., higher than the typically calculated values of 0.06–0.10 for bulk ceria [24], highlighting the existence of a defective ceria structure with the formation of oxygen vacancies on the catalyst surface. The highest ratio values were calculated with the best-performing samples.

The Y $3d_{5/2}$ peak was located at a BE of 157.8 eV and assigned to Y^{3+} ions. The calculated Y/Pd ratio of 0.21 provided important information, as it was very close to the analytical value (0.28), implying a probability of yttrium to occupy sites close to the palladium atoms. The contribution of Y doping to ceria defectivity was demonstrated. The effect was clearly visible when comparing $Ce^{3+}/(Ce^{4+} + Ce_{3+})$ values for Pd/Y-CeAl (0.38) and undoped Pd/CeAl (0.25).

2.2.5. Electron Paramagnetic Resonance (EPR) Measurements

EPR spectra of fresh Pd/CeO_2, Pd/CeAl, Pd/Y-CeAl, and Pd/Al_2O_3 samples are shown in Figure 4. There are two paramagnetic ionic states of palladium, namely Pd^{3+} and Pd^{+} with $4d^7$ and $4d^9$ configurations, respectively. Usually, the Pd^{3+} ions are produced upon oxidation of Pb-containing catalysts at high temperatures. Table 4 summarizes the g values of paramagnetic species in the different investigated samples. Several lines were observed in the EPR spectrum of Pd/CeO_2. Several low-intensity lines with g values ranging from 2.4558 to 2.1130 were recorded in the low-frequency part of the spectrum. These lines were attributed to different species of palladium. EPR lines at g values of 1.9759, 2.2405, and 2.4558 are due to Pd^{3+} ions of rhombic symmetry [25]. Signals with g values of 1.9759 and 1.977 were also recorded in the spectra of Pd/CeAl and Pd/Y-CeAl, respectively. Most probably, these signals can be ascribed to Pd^{3+} ions of different symmetries because the lines observed at a lower magnetic field in the Pd/CeO_2 spectrum with g factors of 2.2405 and 2.4558 were not registered.

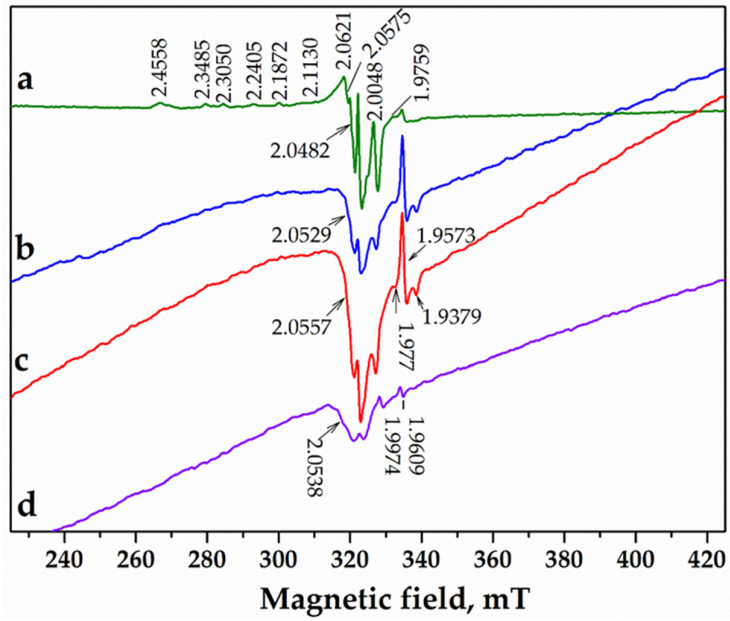


Figure 4. EPR spectra recorded at 123 K: (a) Pd/CeO_2; (b) Pd/CeAl; (c) Pd/Y-CeAl; (d) Pd/Al_2O_3.

Table 4. Signal g values and identified paramagnetic species in fresh samples.

Sample	Chemical Composition (wt.%)					
	Pd^{3+}	Pd^{+}	$Pd^{x+}-O_2$	O_2^-	Ce^{3+}	$Ce^{4+}-O_2^-$
Pd/Al_2O_3			2.0538 1.9974 1.9609	2.0812 2.0661 2.0270	-	-
Pd/CeO_2	2.4558, 2.113, 2.0621, 1.9759	2.3485, 2.3050, 2.2405, 2.1872	2.0575		1.9575, 1.9395	2.0482, 2.0437, 2.0330, 2.0048
Pd/CeAl	1.9759				1.9576, 1.9383	2.0638, 2.0529, 2.0332, 2.0227, 2.0064
Pd/Y-Ce/Al	1.9770		2.0557		1.9573, 1.9379	2.0640, 2.0343, 2.0067

According to the literature, two signals of axial symmetry at $g_{II} = 2.3050$ and $g_{\perp} = 2.1872$ and $g_{II} = 2.3485$ and $g_{\perp} = 2.0482$ in the Pd/CeO_2 sample originated from Pd^{+} ions [25]. The line at a g factor of 2.1130 is also related to the presence of Pd^{+}. In the

central part of the spectrum, several lines with g values ranging from 2.0621 to 2.0048 were recorded. These signals confirmed the presence of adsorbed superoxo species (O_2^-), with one unpaired electron. Oxygen species can be adsorbed onto Ce^{4+} ions or can fill oxygen vacancies, thereby forming surroundings of different symmetries and resulting in different EPR signals [26,27]. Values of g_x for O_2^- are greater than those of the electron g_e factor. The difference is due to the formation of a covalent bond via the overlapping of the oxygen π_y orbital with the 4f orbital of the Ce cation, which has a greater spin orbital coupling constant λ. This kind of oxygen species was found in all spectra.

A signal at g_{II} of about 1.9573 and $g_{\perp}$ of about 1.9379 was found in all ceria-containing samples; exact values are reported in Table 4. According to Soria et al. [28], this signal could be assigned to Ce^{3+} ions associated with anion vacancies; however, it might also originate from F^+ centers [29]. The Ce^{3+} signal intensity was lowest in the Pd/CeO_2 spectrum. It increased with the Pd/CeAl sample and was the most intense for Pd/Y-CeAl. Therefore, Y doping caused an increase in the amount of Ce^{3+} ions. Ceria entities in alumina support might be associated with more dispersed Ce particles at the surface, while O_2^-–Ce^{4+} species are present as less dispersed or aggregate systems. EPR signals with g values of 2.0575, 2.0529, 2.0557, and 2.0538 were observed for Pd/CeO_2, Pd/CeAl, Pd/Y-CeAl, and Pd/Al_2O_3, respectively. Most probably, the signal is related to some palladium species because it is present in all spectra. According to available information in the literature, Pd^{x+}–O adducts yield g_{II} = 1.99, 1.964 and $g_{\perp}$ = 2.05, 2.055 [30]. Therefore, these signals may arise from Pd(I)-O_2 adducts, especially in the Pd/Al_2O_3 sample, where, besides g = 2.0538, signals at g = 1.9974 and g = 1.9609 were also recorded.

Variation of temperature upon recording did not change the shapes of EPR spectra. EPR spectra of Pd/CeO_2 recorded at different temperatures are displayed in Figure 5. A temperature decrease caused only an increase in line intensity. The same behavior was observed with the other samples.

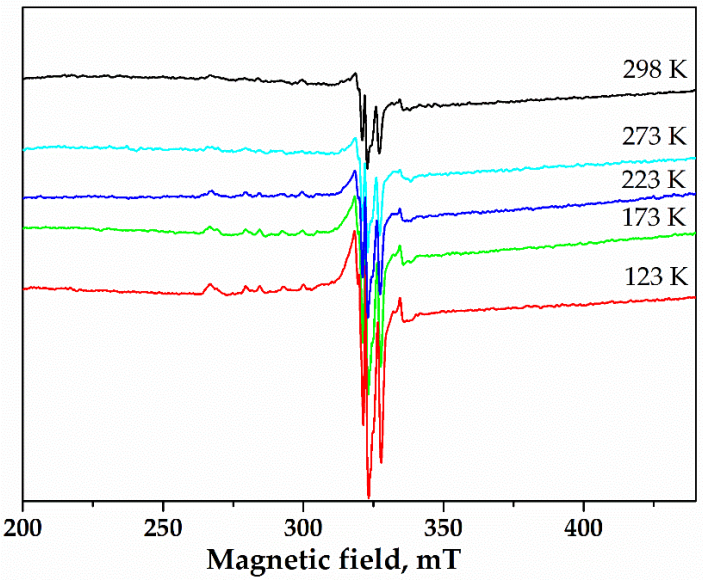


Figure 5. EPR spectra of Pd/CeO_2 recorded at various temperatures.

EPR spectra of Pd/CeO_2, Pd/CeAl, Pd/Y-CeAl, and Pd/Al_2O_3 after methane oxidation reactions are shown in Figure 6. As can be seen, the spectral shapes are almost the same as those of fresh samples. Small changes of the g values were registered, owing to changes in the surrounding atoms during reaction; however, the paramagnetic species causing these changes are the same. Line broadening of the signals positioned at g 2.0529 and 2.0557 in the spectra of Pd/CeAl and Pd/Y-CeAl, respectively, was observed. This

finding implies the formation of palladium magnetic domains of slightly different sizes and quantities attributed to partial particle agglomeration. As a whole, the line intensity of the spectra related to oxygen species decreased, which indicates its depletion during reaction. In the EPR spectra of the fresh Pd/Al_2O_3 sample, the line recorded at a g factor of 1.9609 (Pd^{x+}–O_2^- adducts) disappeared, and a new one with a g factor of 1.9760 (Pd^{3+}) was observed. This is another piece of evidence for oxygen species participating in the methane oxidation reaction. An obvious decrease in Ce^{3+} signal intensity in the Pd/Y-CeAl spectrum was also noticed.

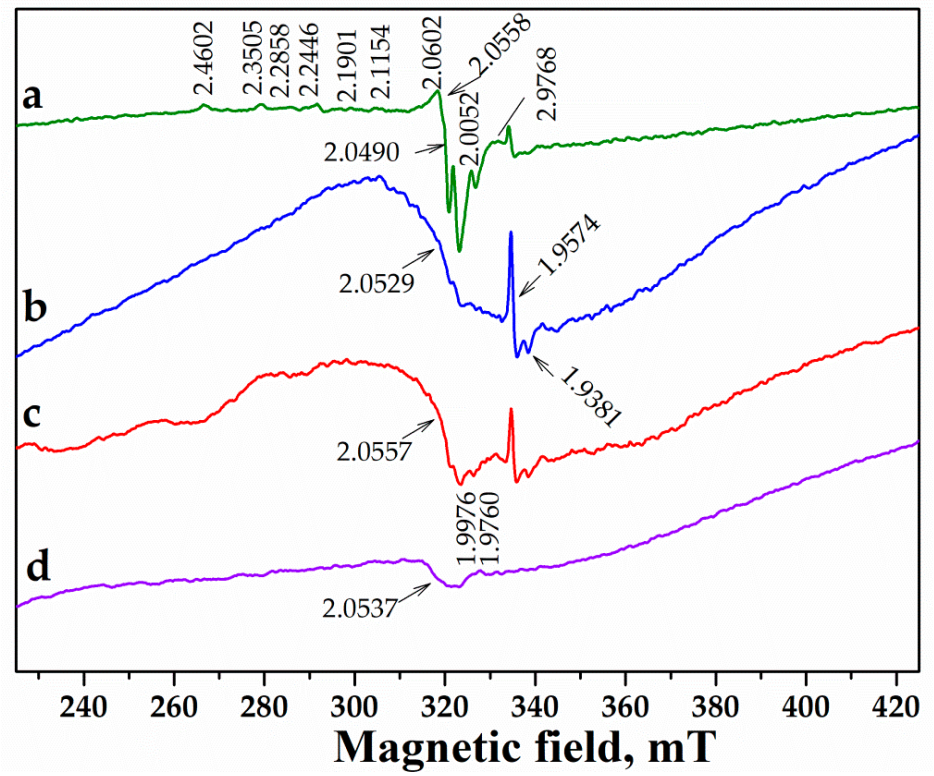


Figure 6. EPR spectra recorded at 123 K: (a) Pd/CeO_2; (b) Pd/CeAl; (c) Pd/Y-CeAl; (d) Pd/Al_2O_3 catalysts after CH_4 oxidation tests.

EPR measurements were also performed on selected samples after CBO tests to shed more light on catalyst stability. The purpose was to detect coke formation on the catalyst surface. Figure 7 shows the spectrum of Pd/CeO_2 because this sample exhibited lower CBO activity in comparison with the other samples. A single EPR line at a g factor of 2.003, which is typical of a carbon-centered radical and coke, was recorded. The EPR spectrum of the best-performing Pd/Y-CeAl catalyst comprises another line at a g value of 2.0023 related to carbon-centered radicals. Two EPR lines with g values of 2.0249 and 2.0054 were also registered in the spectrum, revealing the presence of oxygen species. A well-defined line at a magnetic field of 334–335 mT with a g value of 1.964, assigned to Ce^{3+}, was also observed, focusing on the role of Ce^{3+} for oxygen activation [31]. It should be underlined that such a line was not detected in the Pd/CeO_2 spectrum. This observation highlights a beneficial role of mechanochemical mixing in modifying commercial alumina using highly dispersed ceria nanoparticles.

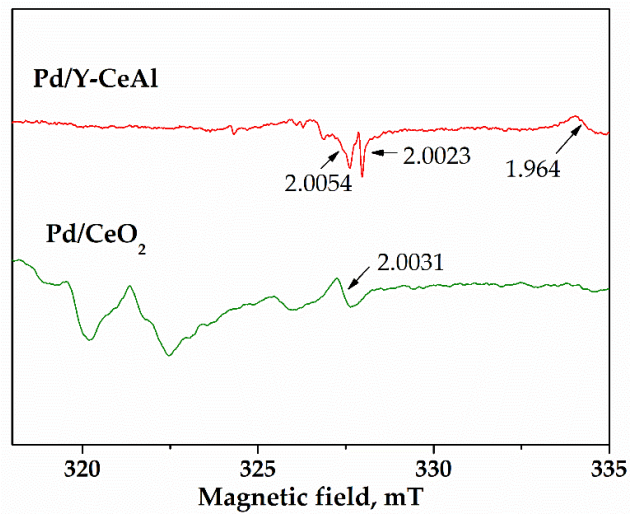


Figure 7. EPR spectra of Pd/CeO_2 and Pd/Y-CeAl catalysts after CBO tests.

2.2.6. Temperature-Programmed Reduction (H_2-TPR) Measurements

Catalyst reducibility was evaluated by TPR with hydrogen. Sample TPR profiles are presented in Figure 8. Hydrogen consumption below 100 °C was observed for all catalysts and attributed to PdO reduction ($PdO \rightarrow Pd^0$). This is in agreement with XPS analysis showing palladium presence as Pd^{2+}. The peak is centered at 21 °C, with Pd/Al_2O_3 and shifts to higher values in the profiles of other catalysts indicating a stronger interaction between palladium oxide and the support [6].

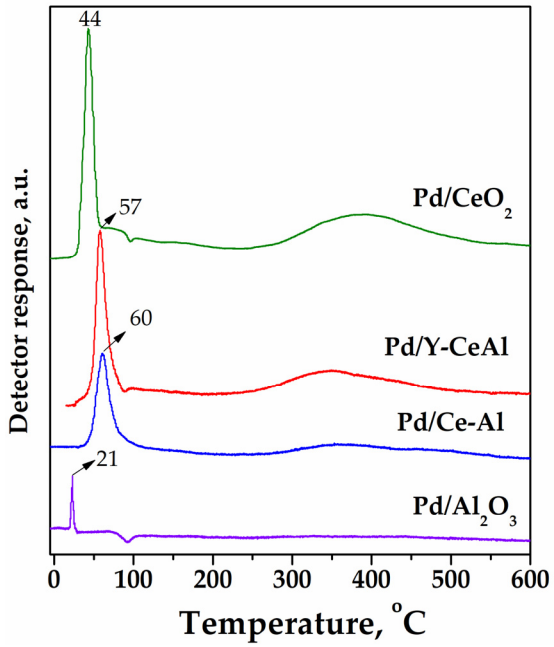


Figure 8. H_2-TPR profiles of studied samples.

TPR profiles of ceria-containing samples contain two peaks. Many works have demonstrated that ceria reduction proceeds in two steps: surface layer reduction at around 500 °C and bulk reduction over 800 °C [32]. Noble metals were reported to facilitate ceria surface layer reduction and boost the first reduction peak at much lower temperatures [33]. Narrow peaks in the temperature range of 44–60 °C included a $PdO \leftrightarrow Pd^0$ redox transfer and oxygen reduction from ceria surface layers in close vicinity to Pd particles. Broad peaks in the temperature range of 300–500 °C could be related to further ceria surface reduction.

The lowest peak intensity was registered for the Pd/CeAl catalyst. A favorable effect of Y doping on ceria surface oxygen mobility and improved reducibility of Pd/Y-CeAl was demonstrated. The highest intensity of the peak with T_{max} at 44 °C in the profile of Pd/CeO_2 could be reasonably explained by considering the highest ceria content. A very weak negative peak at 90 °C in the profile of Pd/Al_2O_3 was attributed to decomposition of Pd β-hydride [34]. Small features related to such decomposition could also be detected at 80−90 °C in the other catalysts; however, their intensity and temperature depend on the catalyst composition and, therefore, on different properties.

Catalyst reducibility was also analyzed based on experimental hydrogen consumption (HC). Values up to 300 °C were calculated because of their relevance to the present study (Table 5). The theoretically calculated HC for PdO reduction was 0.09 mmol·g^{-1}, considering that 1 wt.% Pd matches 1.15 wt.% PdO. After subtraction of this value, HC values for ceria surface layer reduction were 0.34, 0.14, and 0.20 mmol·g^{-1} for Pd/CeO_2, Pd/CeAl, and Pd/Y-CeAl, respectively. In view of the ceria content, the resulting reduction degree was 12, 16, and 23%, accordingly. As already commented above, low-temperature TPR peaks appeared up to 100 °C, and ceria surface layer reduction occurred only close to Pd^0 particles, while $Ce^{4+} \rightarrow Ce^{3+}$ transition for ions far from metallic palladium particles proceeded at 300–500 °C. A similar finding was reported by Gil et al. [35], who assigned a low-temperature TPR peak at 50 °C to Pd-affected ceria surface reduction, followed by further surface reduction above 300 °C.

Table 5. Experimental H_2 consumption during TPR up to 300 °C.

Catalyst	HC (mmol·g^{-1})
Pd/Al_2O_3	0.09
Pd/CeO_2	0.43
Pd/CeAl	0.23
Pd/Y-CeAl	0.29

3. Discussion

The chemical state of palladium is often discussed, owing to its critical role in catalytic methane oxidation activity. Many works have reported PdO as the most active phase and highlighted a favorable correlation between PdO content and catalyst performance [11,36]. However, along with palladium dispersion and oxidation state, the nature of support is of particular importance because it could affect activity by changing the physicochemical properties of palladium species [37]. Cooperation between palladium nanoparticles and the carrier during the catalytic reaction has often been claimed to explain variations in terms of catalytic performance of Pd-based catalysts using different supports. A rational strategy for synthesis of well-performing and economically profitable catalytic materials is based on the exploration of appropriate and cost-effective carriers. In general, a large specific surface area and an abundance of active sites are considered beneficial for high levels of activity of heterogeneous catalysts. Recently, our own studies revealed the suitability of mechanical mixing for the preparation of alumina-supported ceria or Y-doped ceria. In this work, Al_2O_3, CeO_2, CeO_2-Al_2O_3, and Y-doped CeO_2-Al_2O_3 were used as support for palladium catalysts. As shown in Figure 1, three ceria-containing samples showed superior methane oxidation performance, achieving T_{90} at about 300 °C and complete oxidation at 320 °C. Recently, Colussi et al. reviewed advances with respect to the relationship between structural features and reactivity in Pd/CeO_2 catalysts for low-temperature methane combustion [38]. The review focused on the creation of specific structural arrangements, owing to the high degree of nanoscale interaction between Pd/PdO and ceria. A combination of Pd

with different oxidation states, such as Pd and PdO, and ionic entities (PdO_x, Pd^{2+}) was indicated to provide more active sites than bulk PdO. This finding corroborates the clearly high combustion activity exhibited by ceria-containing samples. Evidence for the presence of Pd^{2+} in all palladium-based samples was provided by XP-derived analysis (Table 3, Figure 3). Higher values of the Pd/(Ce + Al) atomic ratio calculated for Pd/CeAl and Pd/Y-CeAl imply a higher dispersion of palladium on the surface of these samples. Two paramagnetic ionic states of palladium, namely Pd^{3+} and Pd^{+}, as well as signals attributed to adsorbed superoxo species (O_2^-) with one unpaired electron, were registered by EPR, confirming the role of ceria in promoting oxygen mobility using Pd ions. The existence of a defective ceria structure with oxygen vacancies forming on the catalyst surface, as revealed by XP and EPR spectral analysis, contributed to significantly higher activity as well. It should be noted that the reciprocal redox behavior of Pd and ceria resulted in the promotion of ceria surface oxygen reduction and enhanced Pd oxidation by ceria. Ceria's unique oxygen exchange properties were considered to explain PdO stabilization because of ceria's ability to hinder PdO reduction and promote Pd reoxidation [11,38] (and references therein). Mechanochemical mixing allowed for the maximization of ceria dispersion on the alumina surface, achieving both a larger interfacial area between deposited Pd nanoparticles and alumina-supported mixed oxides and enhanced oxygen mobility. This close contact favors the generation and movement of active oxygen species on the surface, which are substantial in keeping Pd species in an active oxidized state, thereby facilitating effective CH_4 activation. Chen et al. elucidated active sites for CH_4 oxidation over Pd/CeO_2 and observed CH_4 decomposition over Pd^{2+} in the absence of gas-phase oxygen [39]. Through density functional theory calculations, they revealed the excellent activity of coordinatively unsaturated Pd^{2+} ions and adjacent oxygen atoms in C−H bond breaking. Analysis of the EPR spectra of samples tested in CH_4 oxidation indicated decreased Ce^{3+} signal intensity in the Pd/Y-CeAl spectrum. As described in Section 2.1, Y doping of ceria had no effect on methane conversion. Despite the favorable effect of Y doping on oxygen supply from ceria observed in fresh samples, a possible explanation could be the insignificant contribution of yttrium to oxygen mobility and the formation of vacancies under conditions of CH_4 oxidation.

Although alumina is an inert support and electronic interactions with Pd nanoparticles were not expected, high dispersion of palladium resulted in good performance. It could be hypothesized that lower activity was caused by the deactivation of the active phase, owing to water generated during reaction. As shown in Figure 1a, the T_{50} of Pd/Al_2O_3 was 30 degrees lower than that of Pd/CeO_2, while differences in T_{100} reached 70 degrees.

Some divergences exist in the literature about the role of the palladium oxidation state in benzene oxidation. Some authors have reported that metallic palladium particles enable the formation of more active sites for benzene oxidation relative to PdO [40]. According to Padilla et al., the addition of ceria to $Pd/\gamma\text{-}Al_2O_3$ resulted in the coexistence of PdO species and Pd^0, acting as active sites for benzene oxidation [13]. In contrast to the high CH_4 oxidation activity of all ceria-containing samples, Pd/Al_2O_3 demonstrated higher CBO activity than Pd deposited on reducible CeO_2. Highly dispersed Pd on Al_2O_3 achieved 85% conversion at 100 °C. An explanation could be PdO's ability to provide active oxygen.

The CBO performance of Pd/CeAl and Pd/Y-CeAl resulted from the contribution of both Pd located on ceria or a Y-doped ceria phase and Pd dispersed on alumina. In studying benzene oxidation over zeolite-supported Pd catalysts, He et al. have implied $Pd^{2+}O^{2-}$ reduction by benzene, followed by metallic Pd oxidation with gas-phase oxygen and recovery of the $Pd^{2+}O^{2-}$ species [41]. Such a redox process using gas-phase oxygen is relevant for irreducible supports like alumina; however, in the case of ceria as a reducible support, ceria surface oxygen could be involved in the $Pd^0 \leftrightarrow PdO$ redox transfer. The

beneficial impact of Y doping on oxygen supply from ceria was disclosed by a higher XPS-derived $Ce^{3+}/(Ce^{3+} + Ce^{4+})$ ratio (Table 3) and a higher Ce^{3+} signal intensity in the EPR spectra (Figure 4). Differences in CBO activity could be explained by the role of both palladium and the support for benzene and oxygen activation. Huang et al. reported that the high performance of Pd-based catalysts in VOC oxidation can be attributed to PdO's ability to provide oxygen and the participation of metallic Pd sites in VOC decomposition [3] (and references therein). Benzene adsorption occurs at the Pd surface through π bonds and back donation from the metal to the π^* hydrocarbon orbitals [33].

An explanation of the best performance of Pd-based samples on alumina-supported ceria, particularly on alumina-supported Y-doped ceria, should be based not only on the abovementioned redox $Pd^0 \leftrightarrow PdO$ transfer. Higher surface concentration of Pd and Ce^{3+}, evidenced by XPS analysis, as well as presence of adsorbed O_2^- superoxo species registered in the EPR spectra should also be considered. Moreover, reflections due to the presence of PdO were not detected in XRD patterns of all Pd-containing samples, indicating high dispersion. The role of reducible oxide in improving combustion activity is also worth noting. In spite of the high benzene conversion degree over Pd/Al_2O_3, this catalyst did not achieve complete oxidation of benzene, even at 300 °C. Analyzing the behavior of Pd-based samples on ceria, EPR spectra indicated the formation of coke during the catalytic tests that also negatively affected total benzene conversion. The modification of an irreducible oxide surface using reducible metal oxide appeared favorable in the present case. The advantages of mechanochemical preparation of mixed oxides as carriers of Pd-based catalysts for complete hydrocarbon oxidation as an environmentally friendly and energy-saving synthesis approach were demonstrated.

4. Materials and Methods

4.1. Materials

Commercial γ-Al_2O_3 (Sasol, Brunsbüttel, Germany) was used as support. All reagents used in this study are products of Sigma-Aldrich® solutions (Steinheim, Germany), namely $Ce(NO_3)_3 \cdot 6H_2O$ (cerium nitrate hexahydrate, ≥99.0%), Y_2O_3 (yttrium oxide, ≥99.99%), $Pd(NO_3)_2 \cdot 2H_2O$ (palladium nitrate dehydrate, ~40% Pd basis), and K_2CO_3 (potassium carbonate, ≥99%).

4.2. Catalysts Preparation

Commercial γ-Al_2O_3 and lab-prepared cerium hydroxide were used for CeO_2-Al_2O_3 synthesis. Precipitation of $Ce(NO_3)_3 \cdot 6H_2O$ with K_2CO_3 was carried out at 60 °C and a constant of pH = 9.0, followed by aging at the same temperature for 1 h, washing, and drying at 100 °C. Mechanochemical mixing was performed in an electric mortar (Mortar Grinder RM 200, Retsch GmbH, Haan, Germany) by grinding for 1 min of alumina and calculated $Ce(OH)_3$ amount to provide 30 wt.% CeO_2 in Ce-Al mixed oxide. Then, the mixture was calcined in air at 400 °C for 2 h. Alumina-supported Y-doped ceria support was prepared by the same procedure upon Y_2O_3 addition to the mixture before grinding by using 1 wt.% yttria with respect to the amount of ceria. The notation of mixed oxides is Ce/Al and Y-Ce/Al. Pure CeO_2 was obtained by calcination of cerium hydroxide in air at 400 °C for 2 h.

Pd-based catalysts (1 wt.% Pd) were prepared by deposition–precipitation on carriers suspended in water using ultrasound through the interaction between aqueous solutions of $Pd(NO_3)_2$ and K_2CO_3 at a temperature of 60 °C, a constant of pH = 7, and a stirring speed of 250 rpm. The next steps were aging within 1 h, filtering, washing until the removal of nitrate ions, and thermal treatment at 400 °C for 2 h.

4.3. Catalyst Characterization

Quantitative determination of sample chemical composition was carried out by X-ray fluorescence spectrometry. Analyses were accomplished on a Fischerscope XDAL instrument using WinFTM software (Sindelfingen, Germany) https://www.kks.com.au/helmut_fischer_fischerscope_xrf_x_ray_winftm_v6_software_952_050/, accessed on 12 October 2024.

Sample textural characteristics were determined by N_2 adsorption–desorption isotherms at the liquid nitrogen temperature using a Micromeritics ASAP 2020 apparatus (Norcross, GA, USA). Before measurements, the samples were outgassed at 200 °C for 1 h under vacuum. The specific surface area (S_{BET}) and pore volume (Vp) were calculated using the BET equation applied to the adsorption curve in the standard pressure range of 0.05–0.3 P/P_0. The pore size distribution was obtained by analysis of the desorption curve using the BJH method.

X-ray powder diffraction (XRD) was applied to determine phase composition by means of a Panalytical Empyrean apparatus (Panalytical B.V., Almelo, The Netherlands) equipped with a multichannel detector using Cu Kα 45 kV-40 mA radiation in the 2θ range of 20–115° at a scan step of 0.01° for 20 s.

X-ray photoelectron (XP) spectra were recorded on a VG Microtech ESCA 3000 Multilab instrument (VG Scientific, Sussex, UK) equipped with a dual Mg/Al anode. The experimental procedure is described elsewhere [19]. Sample constant charging was removed by referencing all the energies to the C 1s set at 285.1 eV. Peak analysis was carried out with Casa XPS software (version 2.3.17, Casa Software Ltd. Wilmslow, Cheshire, UK, 2009).

EPR spectra were recorded on a JEOL JES FA100 (JEOL, Tokyo, Japan) ESR spectrometer. The instrument operated in the X band and had a standard T_{011} cylindrical resonator. An ES-DVT4 temperature controller was used to change the resonator temperature and observe EPR spectra at various temperatures. Samples of 100 mg each were loaded into the EPR tubes with the aim of better standardization, and the spectra were recorded under the same conditions: modulation frequency of 100 kHz, microwave power of 1 mW, modulation amplitude of 0.2 mT, time constant of 0.3 s, and sweep time of 4 min. The spectra were temperature-independent. Line intensity was the only variable parameter, which increased with a recorded decrease in temperature.

Temperature-programmed reduction (H_2-TPR) measurements were carried out as previously described [18] using 10% H_2 in Ar at a flow rate of 24 mL min^{-1} and under a temperature increase of 15 °C min^{-1}. The sample quantity was 0.05 cm^3 (particle size of 0.25–0.50 mm) based on the criterion proposed by Monti and Baiker. Hydrogen consumption was calculated by calibration of the thermal conductivity detector using stoichiometric NiO obtained via oxide calcination at 800 °C for 2 h.

4.4. Catalytic Activity Measurements

The samples were examined in the reaction of complete methane oxidation. Measurements were conducted in a flow-type glass reactor at atmospheric pressure (Figure S2) with 0.3 cm^3 charge of the 0.63–0.8 mm fraction and a thin thermocouple in the catalyst bed. A COMECO RT 290 programmable controller (Stuttgart, Germany) monitored reactor temperature. The reaction gas mixture was composed of 1000 ppmv CH_4 and 25 vol.% O_2 and balanced up to 100% with nitrogen, flowing at a total rate of 20,000 h^{-1}. Allborg mass flow controllers were used to keep steady gas flow rates. Gas analysis of the reaction products was performed online using a SICK GMS84 gas analyzer (SICK AG, Waldkirch, Germany) for $CO/CO_2/O_2/CH_4$. Before the reaction, the catalysts were pretreated in a flow of nitrogen and oxygen at 300 °C for 1 h.

The catalytic activity in CBO is expressed as the benzene conversion degree. It was studied within the temperature range of 150–350 °C at atmospheric pressure using a microcatalytic continuous-flow fixed bed reactor connected to a Hewlett Packard 5890 series II gas chromatograph (Agilent, Germany, working with Agilent G2070 Chemstation Software B.04.01, Waldbronn, Germany). The instrument was supplied with a flame ionization detector and capillary column HP Plot Q. A scheme of the catalytic setup used for benzene oxidation measurements is shown in Figure S3. The measurements were carried out using catalyst samples with a 0.5 cm^3 bed volume, a particle size of 0.25–0.50 mm, an inlet benzene concentration of 1314 ppm in air, and a space velocity of 4000 h^{-1}. The benzene conversion degree was calculated by the following equation:

$$C_6H_6 \text{ conversion } (\%) = \{[(C_6H_6)_{in} - (C_6H_6)_{out}]/(C_6H_6)_{in}\} \times 100,$$

where $(C_6H_6)_{in}$ and $(C_6H_6)_{out}$ are the benzene concentration at the reactor inlet and outlet, respectively.

5. Conclusions

The carrier effect on complete methane and benzene oxidation over supported Pd catalysts was found to depend on the hydrocarbon type, owing differences in the mechanisms of interaction between the substrate and Pd^{2+}, namely through the electron-rich π bonding for benzene and through a $C-Pd^{2+}$ interaction in the case of methane. Palladium samples prepared by deposition–precipitation of palladium nitrate on CeO_2, CeO_2-Al_2O_3, and Y-CeO_2-Al_2O_3 exhibited higher CH_4 oxidation activity than Pd/Al_2O_3. Ceria-containing samples reached about 90% CH_4 conversion at 300 °C and complete oxidation at 320 °C vs. 60% at 300 °C and 100% at 390 °C with Pd/Al_2O_3. The adsorption of water generated by the reaction over acidic Al_2O_3 could inhibit CH_4 oxidation, probably by blocking the active sites or due to the formation of less active $Pd(OH)_2$. Pd-based catalysts using CeO_2-Al_2O_3 and especially Y-CeO_2-Al_2O_3 carriers demonstrated superior benzene conversion. Higher Pd and Ce^{3+} surface concentrations, the presence of adsorbed O_2^- superoxo species, and redox $Pd^0 \leftrightarrow PdO$ transfer contributed to the best performance. These results represent an excellent example of the application of mechanochemical preparation of mixed oxides as carriers of Pd-based catalysts for complete hydrocarbon oxidation and highlight the crucial importance of rational catalyst design for efficient catalyst performance.

Supplementary Materials: The following supporting information can be downloaded at: https://www.mdpi.com/article/10.3390/catal15020110/s1, Figure S1: Ce 3d XP spectra of studied samples. Figure S2: Scheme of the catalytic setup used for CH_4 oxidation measurements. Figure S3: Scheme of the catalytic setup used for benzene oxidation measurements. Table S1: Catalytic performance comparison between CH_4 oxidation over Pd-based catalysts developed in this work and reported reference literature. Table S2. Comparison of benzene conversion over Pd-based catalysts developed in this work and reported reference literature. Refs. [6,13,14,16,17,19,21,22,42–47] are cited in Supplementary Materials.

Author Contributions: Conceptualization, T.T. and S.T.; methodology, T.T. and S.T.; formal analysis, B.G., Y.K., P.P., A.M.V. and L.F.L.; investigation, B.G., Y.K., P.P., A.M.V. and L.F.L.; writing—original draft preparation, T.T., Y.K. and S.T.; writing—review and editing, T.T., A.M.V., L.F.L. and S.T. All authors have read and agreed to the published version of the manuscript.

Funding: This work was supported by the European Regional Development Fund under "Research Innovation and Digitization for Smart Transformation" program 2021–2027 under the Project BG16RFPR002-1.014-0006 "National Centre of Excellence Mechatronics and Clean Technologies".

Data Availability Statement: The data presented in this study are available in the article.

Acknowledgments: In this investigation, research equipment of the distributed research infrastructure INFRAMAT supported by the Bulgarian Ministry of Education and Science was used.

Conflicts of Interest: The authors declare no conflicts of interest.

References

1. Moores, F.C. Climate change and air pollution: Exploring the synergies and potential for mitigation in industrializing countries. *Sustainability* **2009**, *1*, 43–54. [CrossRef]
2. Manisalidis, I.; Stavropoulou, E.; Stavropoulos, A.; Bezirtzoglou, E. Environmental and Health Impacts of Air Pollution: A Review. *Front. Public Health* **2020**, *8*, 505570. [CrossRef]
3. Huang, H.; Xu, Y.; Feng, Q.; Leung, D.Y.C. Low temperature catalytic oxidation of volatile organic compounds: A review. *Catal. Sci. Technol.* **2015**, *5*, 2649–2669. [CrossRef]
4. Gelles, T.; Krishnamurthy, A.; Adebayo, B.; Rownaghi, A.; Rezaei, F. Abatement of gaseous volatile organic compounds: A material perspective. *Catal. Today* **2020**, *350*, 3–18. [CrossRef]
5. Guo, Y.; Wen, M.; Li, G.; An, T. Recent advances in VOC elimination by catalytic oxidation technology onto various nanoparticles catalysts: A critical review. *Appl. Catal. B Environ.* **2021**, *281*, 119447. [CrossRef]
6. Todorova, S.; Naydenov, A.; Velinova, R.; Kolev, H.; Larin, A.V.; Stoyanova, D.; Shopska, M.; Tenchev, K.; Stefanov, P. Pd–MeOx/Al_2O_3 (Me = Co, La, Ce) catalysts for methane combustion. *React. Kin. Mech. Catal.* **2019**, *126*, 663–678. [CrossRef]
7. Wang, C.; Xu, Y.; Tang, J. Catalytic methane removal to mitigate its environmental effect. *Sci. China Chem.* **2023**, *66*, 1032–1051. [CrossRef]
8. Liu, R.; Wu, H.; Shi, J.; Xu, X.; Zhao, D.; Ng, Y.H.; Zhang, M.; Liu, S.; Ding, H. Recent progress on catalysts for catalytic oxidation of volatile organic compounds: A review. *Catal. Sci. Technol.* **2022**, *12*, 6945–6991. [CrossRef]
9. Zhang, K.; Ding, H.; Pan, W.; Mu, X.; Qiu, K.; Ma, J.; Zhao, Y.; Song, J.; Zhang, Z. Research progress of a composite metal oxide catalyst for VOC degradation. *Environ. Sci. Technol.* **2022**, *56*, 9220–9236. [CrossRef]
10. Song, S.; Zhang, S.; Zhang, X.; Verma, P.; Wen, M. Advances in catalytic oxidation of volatile organic compounds over Pd-supported catalysts: Recent trends and challenges. *Front. Mater.* **2020**, *7*, 595667. [CrossRef]
11. Monai, M.; Montini, T.; Gorte, R.J.; Fornasiero, P. Catalytic Oxidation of Methane: Pd and Beyond. *Eur. J. Inorg. Chem.* **2018**, *2018*, 2884–2893. [CrossRef]
12. Tabakova, T. State of the Art and Challenges in Complete Benzene Oxidation: A Review. *Molecules* **2024**, *29*, 5484. [CrossRef]
13. Padilla, J.M.; Del Angel, G.; Navarrete, J. Improved Pd/γ-Al_2O_3-Ce catalysts for benzene combustion. *Catal. Today* **2008**, *133–135*, 541–547. [CrossRef]
14. Ramírez-López, R.; Elizalde-Martinez, I.; Balderas-Tapia, L. Complete catalytic oxidation of methane over Pd/CeO_2-Al_2O_3: The influence of different ceria loading. *Catal. Today* **2010**, *150*, 358–362. [CrossRef]
15. Sun, M.; Hu, W.; Yuan, S.; Zhang, H.; Cheng, T.; Wang, J.; Chen, Y. Effect of the loading sequence of CeO_2 and Pd over Al_2O_3 on the catalytic performance of Pd-only close-coupled catalysts. *Mol. Catal.* **2020**, *482*, 100332. [CrossRef]
16. Fertal, D.; Bukhovko, M.; Ding, Y.; Billor, M.; Banerjee, A. Particle size and PdO support interactions in PdO/CeO_2-γAl_2O_3 catalysts and effect on methane combustion. *Catalysts* **2020**, *10*, 976. [CrossRef]
17. Yang, X.; Du, C.; Guo, Y.; Guo, Y.; Wang, L.; Wang, Y.; Zhan, W. Al_2O_3 supported hybrid Pd–CeO_2 colloidal spheres and its enhanced catalytic performances for methane combustion. *J. Rare Earths* **2019**, *37*, 714–719. [CrossRef]
18. Ilieva, L.; Petrova, P.; Liotta, L.F.; Sobczak, J.W.; Lisowski, W.; Kaszkur, Z.; Munteanu, G.; Tabakova, T. Gold catalysts on Y-doped ceria supports for complete benzene oxidation. *Catalysts* **2016**, *6*, 99. [CrossRef]
19. Ilieva, L.; Venezia, A.M.; Petrova, P.; Pantaleo, G.; Liotta, L.F.; Zanella, R.; Kaszkur, Z.; Tabakova, T. Effect of Y modified ceria support in mono and bimetallic Pd-Au catalysts for complete benzene oxidation. *Catalysts* **2018**, *8*, 283. [CrossRef]
20. Venezia, A.M.; Di Carlo, G.; Liotta, L.F.; Pantaleo, G.; Kantcheva, M. Effect of Ti(IV) loading on CH_4 oxidation activity and SO_2 tolerance of Pd catalysts supported on silica SBA-15 and HMS. *Appl. Catal. B Environ.* **2011**, *106*, 529–539. [CrossRef]
21. Tabakova, T.; Ilieva, L.; Petrova, P.; Venezia, A.M.; Avdeev, G.; Zanella, R.; Karakirova, Y. Complete benzene oxidation over mono and bimetallic Au–Pd catalysts supported on Fe-modified ceria. *Chem. Eng. J.* **2015**, *260*, 133–141. [CrossRef]
22. Kalvachev, Y.; Todorova, T.; Kolev, H.; Merker, D.; Popov, C. Benzene oxidation over Pt loaded on fly ash zeolite X. *Catalysts* **2023**, *13*, 1128. [CrossRef]
23. Tabakova, T.; Ivanov, I.; Zanella, R.; Karakirova, Y.; Sobczak, J.W.; Lisowski, W.; Kaszkur, Z.; Ilieva, L. Unraveling the effect of alumina-supported Y-doped ceria composition and method of preparation on the WGS activity of gold catalysts. *Int. J. Hydrog. Energy* **2020**, *45*, 26238–26253. [CrossRef]
24. Liotta, L.F.; Pantaleo, G.; Puleo, F.; Venezia, A.M. Au/CeO_2-SBA-15 catalysts for CO oxidation: Effect of ceria loading on physicochemical properties and catalytic performances. *Catal. Today* **2012**, *187*, 10–19. [CrossRef]

25. Filimonov, I.N.; Ikonnikov, I.A.; Loginov, A.Y. EPR investigation of paramagnetic species on palladium-promoted yttria and lanthana. *J. Chem. Soc. Faraday Trans.* **1994**, *90*, 219–226. [CrossRef]
26. Il'ichev, A.N.; Shashkin, D.P.; Khomenko, T.I.; Fattakhova, Z.T.; Korchak, V.N. Structure and surface properties of ZrO_2, CeO_2, and $Zr_{0.5}Ce_{0.5}O_2$ prepared by a microemulsion method according to X-ray diffraction, TPR, and EPR data. *Kinet. Catal.* **2010**, *51*, 743–753. [CrossRef]
27. Askrabic, S.; Dohcevic-Mitrovic, Z.D.; Araujo, V.D.; Ionita, G.; de Lima, M.M., Jr.; Cantarero, A. F-centre luminescence in nanocrystalline CeO2. *J. Phys. D Appl. Phys.* **2013**, *46*, 495306. [CrossRef]
28. Soria, J.; Martinez-Arias, A.; Coronado, J.M.; Conesa, J.C. Electron paramagnetic resonance spectroscopy study of the adsorption of O_2 and CO on a $Pt/CeO_2/Al_2O_3$ catalyst. *Coll. Surf. A Physicochem. Eng. Asp.* **1996**, *115*, 215–221. [CrossRef]
29. Wang, J.B.; Tai, Y.-L.; Dow, W.-P.; Huang, T.-J. Study of ceria-supported nickel catalyst and effect of yttria doping on carbon dioxide reforming of methane. *Appl. Catal. A Gen.* **2001**, *218*, 69–79. [CrossRef]
30. Taarit, Y.B.; Vedrine, J.C.; Dutel, J.F.; Naccache, C. EPR Investigation of the structure and reactivity of Pd(1) species generated in synthetic mordenite-type zeolite. *J. Magn. Reson.* **1978**, *31*, 251–257. [CrossRef]
31. Ge, L.; Chen, T.; Liu, Z.; Chen, F. The effect of gold loading on the catalytic oxidation performance of CeO_2/H_2O_2 system. *Catal. Today* **2014**, *224*, 209–215. [CrossRef]
32. Yao, H.C.; Yao, Y.F.Y. Ceria in automotive exhaust catalysts: I. Oxygen storage. *J. Catal.* **1984**, *86*, 254–265. [CrossRef]
33. Liotta, L.F. Catalytic oxidation of volatile organic compounds on supported noble metals. *Appl. Catal. B Environ.* **2010**, *100*, 403–412. [CrossRef]
34. Hosseini, M.; Siffert, S.; Tidahy, H.L.; Cousin, R.; Lamonier, J.-F.; Aboukais, A.; Vantomme, A.; Roussel, M.; Su, B.-L. Promotional effect of gold added to palladium supported on a new mesoporous TiO_2 for total oxidation of volatile organic compounds. *Catal. Today* **2007**, *122*, 391–396. [CrossRef]
35. Gil, S.; Garcia-Vargas, J.M.; Liotta, L.F.; Pantaleo, G.; Ousmane, M.; Retailleau, L.; Giroir-Fendler, A. Catalytic oxidation of propene over Pd catalysts supported on CeO_2, TiO_2, Al_2O_3 and M/Al_2O_3 oxides (M = Ce, Ti, Fe, Mn). *Catalysts* **2015**, *5*, 671–689. [CrossRef]
36. Wang, W.; Zhou, W.; Li, W.; Xiong, X.; Wang, Y.; Cheng, K.; Kang, J.; Zhang, Q.; Wang, Y. In-situ confinement of ultrasmall palladium nanoparticles in silicalite-1 for methane combustion with excellent activity and hydrothermal stability. *Appl. Catal. B Environ.* **2020**, *276*, 119142. [CrossRef]
37. Wang, X.; Liu, Y.; Ge, W.; Xu, Y.; Jia, H.; Li, Q. Complete oxidation of lean methane over metal oxide supported Pd catalysts: Current advancement and future perspectives. *J. Environ. Chem. Eng.* **2023**, *11*, 110712. [CrossRef]
38. Colussi, S.; Fornasiero, P.; Trovarelli, A. Structure-activity relationship in Pd/CeO_2 methane oxidation catalysts. *Chin. J. Catal.* **2020**, *41*, 938–950. [CrossRef]
39. Chen, S.; Li, S.; You, R.; Guo, Z.; Wang, F.; Li, G.; Yuan, W.; Zhu, B.; Gao, Y.; Zhang, Z.; et al. Elucidation of active sites for CH_4 catalytic oxidation over Pd/CeO_2 via tailoring metal-support interactions. *ACS Catal.* **2021**, *11*, 5666–5677. [CrossRef]
40. Kim, S.C.; Shim, W.G. Properties and performance of Pd based catalysts for catalytic oxidation of volatile organic compounds. *Appl. Catal. B Environ.* **2009**, *92*, 429–436. [CrossRef]
41. He, C.; Li, J.; Li, P.; Cheng, J.; Hao, Z.; Xu, Z.-P. Comprehensive investigation of Pd/ZSM-5/MCM-48 composite catalysts with enhanced activity and stability for benzene oxidation. *Appl. Catal. B Environ.* **2010**, *96*, 466–475. [CrossRef]
42. Liu, J.; Wang, H.; Chen, Y.; Yang, M.; Wu, Y. Effects of pretreatment atmospheres on the catalytic performance of $Pd/\gamma\text{-}Al_2O_3$ catalyst in benzene degradation. *Catal. Commun.* **2014**, *46*, 11–16. [CrossRef]
43. Kang, S.; Wang, M.; Zhu, N.; Wang, C.; Deng, H.; He, H. Significant enhancement in water resistance of Pd/Al_2O_3 catalyst for benzene oxidation by Na addition. *Chin. Chem. Lett.* **2019**, *30*, 1450–1454. [CrossRef]
44. He, Z.; He, Z.; Wang, D.; Bo, Q.; Fan, T.; Jiang, Y. Mo-modified Pd/Al_2O_3 catalysts for benzene catalytic combustion. *J. Environ. Sci.* **2014**, *26*, 1481–1487. [CrossRef]
45. Guo, Y.; Gao, Y.; Li, X.; Zhuang, G.; Wang, K.; Zheng, Y.; Sun, D.; Huang, J.; Li, Q. Catalytic benzene oxidation by biogenic Pd nanoparticles over 3D-ordered mesoporous CeO_2. *Chem. Eng. J.* **2019**, *362*, 41–52. [CrossRef]
46. Zhao, B.; Cheng, Z.; Zheng, J.; Wang, Z.; Zuo, S. Synthesis of $C_{21}H_{38}ClN$ assisted Si pillared clays and the effects of CeO_2 addition on its supported palladium catalyst for benzene oxidation. *Catal. Lett.* **2021**, *151*, 3287–3297. [CrossRef]
47. Zuo, S.; Du, Y.; Liu, F.; Han, D.; Qi, C. Influence of ceria promoter on shell-powder-supported Pd catalyst for the complete oxidation of benzene. *Appl. Catal. A Gen.* **2013**, *451*, 65–70. [CrossRef]

Disclaimer/Publisher's Note: The statements, opinions and data contained in all publications are solely those of the individual author(s) and contributor(s) and not of MDPI and/or the editor(s). MDPI and/or the editor(s) disclaim responsibility for any injury to people or property resulting from any ideas, methods, instructions or products referred to in the content.